

Emergent bright excitons with Rashba spin-orbit coupling in atomic monolayersJiayu David Cao ^{1,*}, Gaofeng Xu ², Benedikt Scharf ³, Konstantin Denisov ¹ and Igor Žutić ^{1,†}¹*Department of Physics, University at Buffalo, State University of New York, Buffalo, New York 14260, USA*²*Department of Physics, Hangzhou Dianzi University, Hangzhou, Zhejiang 310018, China*³*Institute for Theoretical Physics and Astrophysics and Würzburg-Dresden Cluster of Excellence *ct.qmat*, University of Würzburg, Am Hubland, 97074 Würzburg, Germany*

(Received 31 August 2023; revised 31 December 2023; accepted 11 January 2024; published 6 February 2024; corrected 20 February 2024)

Optical properties in van der Waals heterostructures based on monolayer transition-metal dichalcogenides (TMDs) are often dominated by excitonic transitions. While intrinsic spin-orbit coupling (SOC) and an isotropic band structure are typically studied in TMDs, in their heterostructures Rashba SOC and trigonal warping (TW), resulting in bands with threefold anisotropy, are also present. By considering a low-energy effective Hamiltonian and Bethe-Salpeter equation, we study the effect of Rashba SOC and TW on the band structure and absorption spectra. Rashba SOC is predicted to lead to emergent excitons, which are identified as an admixture between $1s$ and $2p$ symmetries. In contrast, for experimentally relevant values, TW has only a negligible effect on the absorption spectrum. These findings could guide experimental demonstrations of emergent bright excitons and further studies of the proximity effects in van der Waals heterostructure.

DOI: [10.1103/PhysRevB.109.085407](https://doi.org/10.1103/PhysRevB.109.085407)**I. INTRODUCTION**

There is a growing class of atomically thin van der Waals (vdW) materials with striking optical properties which, unlike their bulk counterparts, can be highly tunable and have strong Coulomb interactions [1–8]. These properties are exemplified in transition-metal dichalcogenides (TMDs) with direct band gaps and efficient light emission, valley-dependent helicity of optical transitions, broken inversion symmetry together with a strong intrinsic spin-orbit coupling (SOC), and tightly bound excitons, dominating the optical response [9–12].

In vdW heterostructures, as a platform to transform their atomically thin materials through proximity effects, the role of TMDs is twofold. TMDs acquire magnetic, superconducting, enhanced SOC, charge-density wave, or topological properties [13–22], while they also transform the neighboring regions, for example by altering their magnetic properties [23,24]. Since the resulting change in the excitonic spectrum of atomically thin materials is a probe for magnetic proximity effects or a tunable band topology [25–32], it is crucial to establish a description of these systems beyond the single-particle picture [26].

In this work, we focus on the evolution of the optical absorption in monolayer (ML) TMDs with Rashba SOC and trigonal warping (TW), which are inherent to TMDs and their vdWs heterostructures, but whose combined role on excitons remains largely unexplored [1]. Similar to the extensively studied two-dimensional electron gas [33,34], Rashba SOC occurs in TMD systems with broken structural inversion symmetry, and its strength can be tuned by an externally applied

electric field. In TMDs this symmetry breaking is readily realized due to a substrate [shown in Fig. 1(a)] or in ML Janus TMDs [3,35].

The presence of TW in TMDs removes the usually assumed isotropic dispersion near the K/K' valleys and introduces a threefold symmetry accompanied with strong nonlinear optical properties [36–38]. We base our approach on the Bethe-Salpeter equations to include strong Coulomb interaction that, with reduced screening, can lead to exciton binding energies of up to 0.5 eV, orders of magnitude larger than in bulk semiconductors [1].

In Fig. 1(a) we illustrate the considered system, illuminated by light. The corresponding absorption spectrum in Fig. 1(b), shown without Rashba SOC and TW, has two main peaks indicating the A and B excitons, bound electron-hole pairs that can be described within the low-energy four-band model, shown in Fig. 1(c) for a single valley. In semiconducting ML TMDs (MX_2 , $M = \text{Mo, W}$; $X = \text{S, Se, Te}$), the SOC splitting is larger for the valence band (VB) than the conduction band (CB), of which the spin ordering is opposite for $M = \text{Mo}$ and W [1,9].

The lower energy A exciton corresponds to the bound state formed from the hole in the upper valence subband (VB2) and the electron in the lower conducting subband (CB1), while the B exciton is formed from the VB1 and CB2 subbands, shown in the second diagram in Fig. 1(c). Unlike these bright A and B excitons that correspond to the optically allowed dipole transitions in Fig. 1(c), $2p$ excitons (third and fourth diagram) and spin-forbidden B' series excitons (first and third diagram) are optically forbidden and termed dark. Here the notation for various excitons, $1s$, $2p$, ... is derived from their similarity with the hydrogenlike states below the band gap [39], while the CB ordering corresponds to MoX_2 TMDs.

*jiayuc@buffalo.edu

†zigor@buffalo.edu

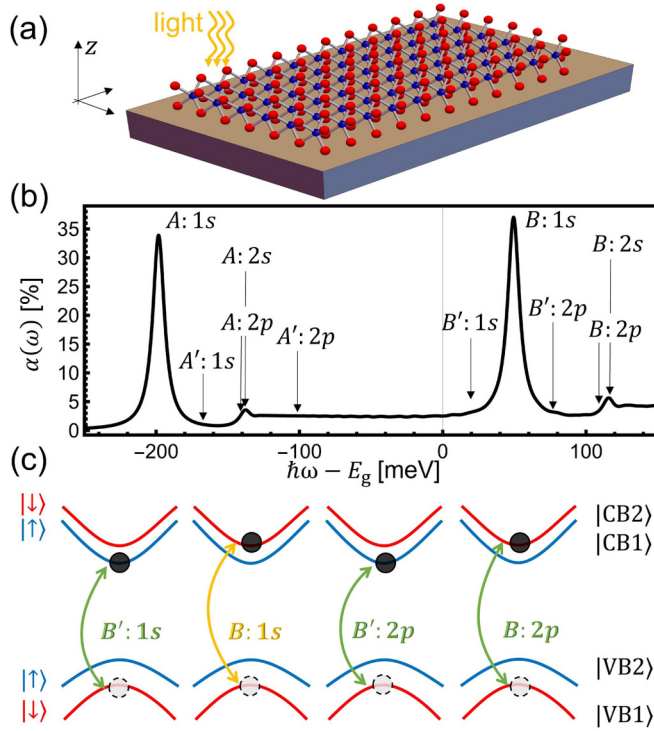


FIG. 1. (a) Schematic of an atomic ML on a substrate. (b) Absorption spectrum computed numerically without trigonal warping or Rashba SOC, based on the Bethe-Salpeter equation described in Sec. II. The absorption peaks denote various excitons: A (A') are formed from CB1 (CB2) and VB2, while B (B') are formed from CB2 (CB1) and VB1, where CB1,2 (VB1,2) are conduction (valence) subbands with spins marked by arrows. (c) Examples of B and B' excitons in ascending energy order in the K valley. Yellow (green) arrows: bright (dark) excitons. Black (gray) circles: electrons (holes).

Our calculated results for the absorption spectrum in Fig. 1 contain basic properties about the bright and dark excitons in TMDs and provide a reference point to identify a possible influence of Rashba SOC and TW. While Rashba SOC is absent in nonpolar ML TMDs (MX_2 , $M = \text{Mo, W}$; $X = \text{S, Se, Te}$), where the two planes of X chalcogen atoms are symmetrically surrounding the plane of M metallic atoms, it is inherent and can be very strong in polar ML Janus TMDs (MXY , $M = \text{Mo, W}$; $X = \text{S, Se, Te}$; $Y \neq X$), induced by the broken out-of-plane mirror symmetry [3]. TW is predicted for graphene and its multilayers [40,41], as well as in ML TMDs and Janus TMDs [42–45]. However, in studies of excitons in atomic MLs with a hexagonal lattice, the band structure at the K/K' valleys is usually modeled assuming an isotropic dispersion which neglects TW.

An additional motivation for our work comes from recognizing that excitonic features in atomic MLs provide fingerprints for proximitized materials, for example, modified by magnetism, charge density wave, or tunable band topology [16,26,27]. Our findings on the role of Rashba SOC and TW could also guide future studies in more complex systems, including the interplay of multiple proximity effects. Even for seemingly well-understood magnetic proximity effects, the common picture is incomplete. In contrast to the assumed similarity of magnetic proximity with an applied magnetic

field leading to a spin splitting in the TMD, the modification of the excitonic spectrum in MoSe_2 placed on top of a magnetic insulator, CrBr_3 , reveals a valley-dependent shift indicating that the proximity-induced spin splitting is valley-dependent [46,47]. Further measurements of excitonic features of other atomic MLs may reveal even more surprises.

Following this Introduction, in Sec. II we outline our theoretical framework using a low-energy Hamiltonian and Bethe-Salpeter equation to describe excitons in ML TMDs. In Sec. III we discuss the results for our computational system, based on ML MoTe_2 on a substrate with a large dielectric constant. Specifically, we focus on the modifications of the optical properties with Rashba SOC and TW. While Rashba SOC can lead to pronounced effects and unexplored emergent excitons, the role of TW has only a very modest effect on the absorption spectra. In Sec. IV we provide our conclusions and an outlook.

II. THEORETICAL MODEL

A. Low-energy effective Hamiltonian

In the absence of broken time-reversal symmetry and net magnetization, for a description of a ML TMD on a substrate as shown in Fig. 1(a), it is sufficient to consider one of the valleys, K , while the behavior of the other valley, K' , is related through the time-reversal operation. For bands with a two-dimensional (2D) representation, the SOC Hamiltonian can be written as $H_{\text{SO}} = \mathbf{\Omega}(\mathbf{k}) \cdot \mathbf{s}$ using the SOC field $\mathbf{\Omega}(\mathbf{k})$ [15,34,48], where \mathbf{k} is the wave vector and \mathbf{s} is the vector of spin Pauli matrices. In ML TMDs, this leads to $\mathbf{\Omega}(\mathbf{k}) = \lambda(\mathbf{k})\hat{z}$, where $\lambda(\mathbf{k})$ is odd in \mathbf{k} , and \hat{z} is the unit vector normal to the ML plane. At the K point, $\lambda(\mathbf{k})$ reduces to the values $\lambda_{c(v)}$ in the CB (VB). Within the single-particle picture, the total low-energy Hamiltonian is given by [44]

$$H_{\text{tot}} = H_0 + H_R + H_{\text{TW}}, \quad (1)$$

which is a sum of the “bare” ML-TMD, Rashba SOC, and TW terms [43,44], respectively. Here the first term in the four-band model that includes an inherent SOC can be expressed as

$$H_0 = \hbar v_F(k_x \sigma_x \tau_z + k_y \sigma_y) + (E_g/2)\sigma_z + \tau_z s_z [\lambda_c(1 + \sigma_z)/2 + \lambda_v(1 - \sigma_z)/2], \quad (2)$$

where σ_i and τ_i denote Pauli matrices for the CB or VB, and K/K' valley, respectively. v_F is the Fermi velocity, $k_{x,y}$ are wave vectors measured from K/K' , E_g is the band gap, and $2\lambda_c$ and $2\lambda_v$ are the SOC splitting in the CB and VB. With λ_R and κ describing the strength of Rashba SOC and TW, we have

$$H_R = \lambda_R(s_y \sigma_x \tau_z - s_x \sigma_y) \quad (3)$$

and

$$H_{\text{TW}} = \kappa [(k_x^2 - k_y^2)\sigma_x - \tau_z 2k_x k_y \sigma_y]. \quad (4)$$

Equations (1)–(4) describe the single-particle band structure of our system, which serves as a starting point for our many-body calculations.

B. Bethe-Salpeter equation and excitons

From the resulting single-particle description $H_{\text{tot}}^{\tau} \eta_{nk}^{\tau} = \epsilon_n^{\tau}(\mathbf{k}) \eta_{nk}^{\tau}$, with the eigenenergies ϵ_n^{τ} and the corresponding eigenstates η_{nk}^{τ} as the basis, we take into account many-body effects through the Bethe-Salpeter equation (BSE) [26,49–52] to study excitons in the presence of Rashba SOC and TW,

$$[\Omega^{S,\tau} - \epsilon_c^{\tau}(\mathbf{k}) + \epsilon_v^{\tau}(\mathbf{k})] \mathcal{A}_{vck}^{S\tau} = \sum_{v'c'k'} \mathcal{K}_{vck,v'c'k'}^{\tau} \mathcal{A}_{v'c'k'}^{S\tau}, \quad (5)$$

where in a given valley τ the band index $n = c(v)$ denotes one of the two CB (VB) subbands. $\Omega^{S,\tau}$ is the energy of an exciton in the state S , given by the wave function $|\Psi_S^{\tau}\rangle = \sum_{vck} \mathcal{A}_{vck}^{S\tau} \hat{c}_{\tau ck}^{\dagger} \hat{c}_{\tau vk} |\text{GS}\rangle$ with coefficients $\mathcal{A}_{vck}^{S\tau}$, the creation (annihilation) operator of an electron in a CB c (VB v) $\hat{c}_{\tau ck}^{\dagger}$ ($\hat{c}_{\tau vk}$) in a valley τ , and the ground state $|\text{GS}\rangle$ with fully occupied VBs and empty CBs. The kernel $\mathcal{K}_{vck,v'c'k'}^{\tau}$ includes the Coulomb interaction between electrons in the layer, determined from the dielectric environment, geometry, and form factors calculated from η_{nk}^{τ} [26,53–55]. While $\mathcal{K}_{vck,v'c'k'}^{\tau} = \mathcal{K}_{vck,v'c'k'}^{d,\tau} + \mathcal{K}_{vck,v'c'k'}^{x,\tau}$ consists of the direct and exchange terms [26,51], since we do not consider intervalley transitions, the exchange term vanishes due to the orthogonality of the eigenspinors η_{nk}^{τ} [26,27]. The interaction kernel only contains the direct term of the form [1,26]

$$\mathcal{K}_{vck,v'c'k'}^{\tau} = -\frac{V(\mathbf{q} \equiv \mathbf{k} - \mathbf{k}') f_{cc'}^{\tau}(\mathbf{k}, \mathbf{k}') f_{v'v}^{\tau}(\mathbf{k}', \mathbf{k})}{A}, \quad (6)$$

where $V(\mathbf{q} \equiv \mathbf{k} - \mathbf{k}')$ is the Fourier transform of the bare Coulomb potential determined from the dielectric environment, while the form factors $f_{nn'}^{\tau}(\mathbf{k}, \mathbf{k}') = [\eta_{nk}^{\tau}]^{\dagger} \eta_{n'k'}^{\tau}$ are calculated from the single-particle states, and A is the unit area. In the absence of Rashba SOC, spin is a good quantum number, so the form factors vanish for coupling between different CBs (VBs), and the CBs (VBs) decouple in a kernel $\mathcal{K}_{vck,v'c'k'}^{\tau}$. The bare Coulomb potential is determined only from the dielectric environment and can be obtained from the Poisson equation. Correspondingly, $V(\mathbf{q})$ between two electrons in the xy -plane ($z = z' = 0$) for a ML TMD of thickness d is given by [26,56,57]

$$V(\mathbf{q}) \approx \frac{2\pi e^2}{\epsilon q + r_0 q^2}, \quad (7)$$

where this expression follows from an expansion in powers of qd , which is very accurate for a thin layer, $qd \ll 1$. Here $\epsilon = (\epsilon_t + \epsilon_b)/2$ is the average (background) dielectric constant of the top and bottom materials surrounding the ML TMD. The ML polarizability is

$$r_0 = \frac{\tilde{\epsilon} d}{2} \left(1 - \frac{\epsilon_t^2 + \epsilon_b^2}{2\tilde{\epsilon}^2} \right), \quad (8)$$

where $\tilde{\epsilon}$ is the dielectric constant of the single atomic layer. In the limit of $\epsilon_{t/b} \ll \tilde{\epsilon}$, $r_0 = \tilde{\epsilon} d/2$ [53,54]. The interaction given by Eq. (7) has proven to be successful in capturing the excitonic properties of ML-TMDs [58,59].

While excitons in TMDs deviate from 2D hydrogen due to screening, they can still be labeled as $1s$, $2s$, $2p$, etc., based on their symmetry [51,59–61]. To classify the excitons according to their symmetries, we study the real-space exciton wave

function

$$\Psi^{S,\tau}(\mathbf{r}_e - \mathbf{r}_h) = \sum_{vck} \mathcal{A}_{vck}^{S\tau} \psi_{ck}^{\tau}(\mathbf{r}_e) \psi_{vk}^{\tau*}(\mathbf{r}_h), \quad (9)$$

where $\psi_{ck}^{\tau}(\mathbf{r}_e) \psi_{vk}^{\tau*}(\mathbf{r}_h) = e^{i\mathbf{k} \cdot (\mathbf{r}_e - \mathbf{r}_h)} \sum_{i,j} [\eta_{ck}^{\tau} \eta_{vk}^{\tau}]_{ij} / A$, and \mathbf{r}_e (\mathbf{r}_h) are the electron (hole) coordinates. The single-particle eigenstate wave function can be calculated as $\psi_{nk}^{\tau}(\mathbf{r}) = e^{i\mathbf{k} \cdot \mathbf{r}} \sum_m [\eta_{nk}^{\tau}]_m(\mathbf{r} | m \mathbf{k}) / \sqrt{A}$, where m is the subband index. Since we focus on the exciton symmetry, we assume a constant periodic part $\langle \mathbf{r} | m \mathbf{k} \rangle$ of the Bloch function for the calculation. This simplification removes the crystal site dependence of the exciton wave function, consistent with our low-energy Hamiltonian. Thus the wave function in our work is actually the exciton envelope wave function [62]. As noted for Eq. (6), without Rashba SOC, the CBs (VBs) in $\mathcal{K}_{vck,v'c'k'}^{\tau}$ decouple. Thus A and B exciton series are independent.

Unlike in 2D hydrogen, a state with higher angular momentum can have a larger binding energy than a state with lower angular momentum. For example, the first few low-energy states are $1s$, $2p$, and $2s$, as shown in Fig. 1(b). This different ordering is already well known [59,61] and is expected since the spatial dependence of the screened Coulomb interaction in TMDs deviates from the hydrogenic form. However, TMD excitons obey identical selection rules to 2D hydrogen. For example, s -type excitons are bright, p -type excitons are dark [59]. Signatures of bright excitons are given in the absorption spectrum

$$\alpha^{\pm}(\omega) = \frac{4e^2 \pi^2}{c\omega} \frac{1}{A} \sum_{S\tau} \left| \sum_{vck} \mathcal{D}_{vck}^{\tau,\pm} \mathcal{A}_{vck}^{S\tau} \right|^2 \delta(\hbar\omega - \Omega^S), \quad (10)$$

where ω is the photon frequency of light propagating along the $-\hat{z}$ direction, and c is the speed of the light. The single-particle velocity matrix elements are given by $\mathcal{D}_{vck}^{\tau,\pm} = [\eta_{vk}^{\tau}]^{\dagger} \hat{v}_{\pm} \eta_{ck}^{\tau}$ for left/right circularly polarized light (helicity eigenstates) with $\hat{v}_{\pm} = (\hat{v}_x \pm i\hat{v}_y) / \sqrt{2}$, $\hat{v}_{x/y} = \partial H_{\text{tot}} / \partial (\hbar k_{x/y})$. A zero sum $\sum_{vck} \mathcal{D}_{vck}^{\tau,\pm} \mathcal{A}_{vck}^{S\tau}$ indicates a dark exciton. The δ function is modeled by a Lorentzian with broadening Γ , where a smaller Γ is necessary to identify excited states of A , B series, with the cost of a denser k -mesh and longer computational times.

III. RESULTS

A. Computational system

To explore the influence of Rashba and TW, we consider the system air/MoTe₂/substrate, where MoTe₂ is described by the band gap $E_g = 1.4$ eV, which matches the experimentally observed peak position at ~ 1.2 eV for MoTe₂ [63]. The Fermi velocity is $v_F = 3.28 \times 10^5$ m/s, and $\lambda_c = -18$ meV and $\lambda_v = 110$ meV determine the SOC splittings [recall Eq. (2)], while the lattice constant is $a_0 = 3.52$ Å for MoTe₂ [26,64]. As in Eq. (4), TW is parametrized by $\kappa = -1.1$ eV Å [43,44]. The presence of a substrate leads to Rashba SOC, which can be as large as $\lambda_R = 72$ meV [65], which guides the range of Rashba SOC we examine. Specifically, $\lambda_R = 50$ meV is large enough to clearly show the emergent excitons. Additionally, a substrate influences the background dielectric constant, here taken as $\epsilon = 12.45$ to be consistent with a HfO₂ substrate [66], which is used with various TMDs [67,68] and $r_0 = 6.3$ nm.

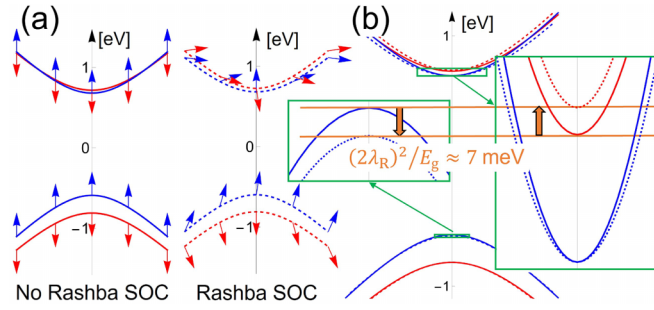


FIG. 2. (a) Schematic single-particle band structure and spin textures (denoted by arrows) in the K valley with Rashba SOC strength $\lambda_R = 0, 50$ meV. The other parameters are given in Sec. III A. (b) Magnified band edges with the indicated Rashba-induced blue shift, where E_g is the band gap.

Together, ε and r_0 characterize the polarization of our computational system [26,58,59].

For our numerical calculations, an $N \times N$ k -grid with a spacing of $\Delta k = 2\pi/(Na_0)$ in each direction is used. We limit our calculation by an upper cutoff energy $E_{\text{cut}} = E_g/2 + 500$ meV. To ensure convergence in our numerical calculations, we have used $N = 250$. A broadening $\Gamma = 5$ meV is used for the spectrum, which is large enough for a smooth curve, while small enough to identify possible new excitonic features arising from Rashba SOC.

B. Rashba SOC and emergent excitons

1. Single-particle description

While the absorption spectra in TMDs are typically dominated by excitons and therefore are not captured by the single-particle description, some of the modifications of excitonic properties with Rashba SOC can already be inferred from the trends present at the single-particle picture. To show this, we compare the band structures and the corresponding spin textures at the K valley with and without Rashba SOC, showing a simple situation in which the collinear spins ensure that spin is a good quantum number. In Fig. 2(a) we see that the interplay between intrinsic and Rashba SOC leads to noncollinear spin textures. The resulting absence of a single spin quantization axis suggests that the optical selection rules for dipole transitions are relaxed and that initially forbidden dark excitons can become bright and optically allowed.

In our case, we have different types of “dark” excitons: the spin-forbidden excitons (A' and B') and p -shell spin-allowed excitons (A and B), which can be active, though, in two-photon processes [69]. Relaxing the spin quantization axis, in general, can lead to the optical brightness of both of these excitonic states. For instance, within the single-particle picture, the transitions between spin-split energy levels with opposite spin states can be allowed in the presence of finite SOC due to the electric dipole spin resonance [70]. This process can make A' : and B' : s -shell excitons optically bright; arising microscopically from SOC-assisted interband spin-flip transitions [71]. However, as we demonstrate below, at sufficiently large magnitudes of SOC, the dominant role for the absorption spectra comes from a different effect: the mixing of s -shell and p -shell excitons.

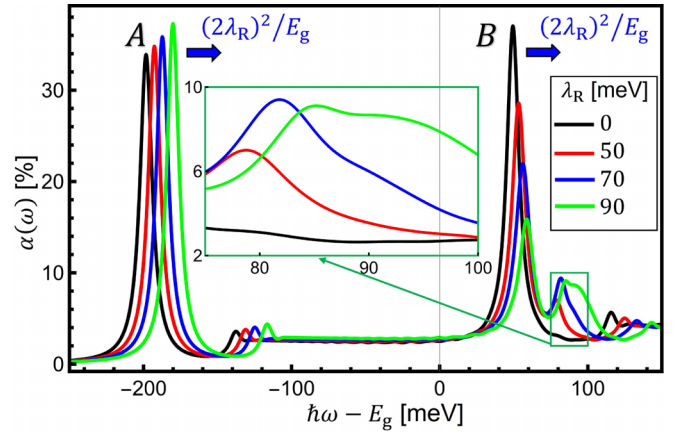


FIG. 3. Absorption spectra for an air/MoTe₂/substrate system with different strengths of Rashba SOC. Blue arrows: the energy shifts of A and B excitons, expected from the single-particle analysis. The inset highlights the emergence of Rashba-induced peaks. The other parameters are given in Sec. III A.

This situation is analogous to TMDs in the absence of Rashba SOC on a magnetic substrate with an in-plane magnetization [26]. From the magnified view of the CB and VB near the K valley, in Fig. 2(b) we can anticipate two more trends for excitons with the increase in λ_R : (i) The absorption peaks will blueshift, which can be understood as a result of the indicated moving down/up of VB2/CB2, by $(2\lambda_R)^2/E_g$. (ii) The heights of the excitonic A peak will slightly increase since CB1 and VB2 become flatter. The states closer to band edges dominate both single-particle and many-body absorption spectra [72]. Therefore, a higher density of states around band edges caused by flatter bands leads to an enhanced absorption for the corresponding transition.

2. Absorption spectrum: Emergent bright excitons

We next turn to the calculation of absorption spectra from Eq. (10) using the BSE [Eq. (5)] to include the effects of strong Coulomb interaction and explore various trends in the excitonic peaks with Rashba SOC. The importance of using the BSE can be readily seen from the comparison with our results for a single-particle absorption, which are calculated for the same air/MoTe₂/substrate system, discussed further in the Appendix (Fig. 8). At the single-particle level, excitonic peaks are absent. The exciton binding energies, ≈ 70 meV (Fig. 7), are responsible for the redshift of the A and B peaks, as compared to what would be expected from the corresponding energies of the CB and VB. For our considered system, this redshift is much larger than the blueshift due to Rashba SOC, which has been inferred from the single-particle analysis in Fig. 2(b) and marked with arrows in Fig. 3.

Several striking features can be readily seen in Fig. 3. First of all, we do not observe a noticeable rise of the absorption due to the brightness of the s -shell spin forbidden excitons A' : $1s$ and B' : $1s$ that might have been expected from the single-particle interband spin-flip mechanism [71]. Instead, we see an additional emergent absorption peak with energy slightly higher than the B : $1s$ exciton but smaller than the B : $2s$ transition. Its evolution is highlighted in the inset,

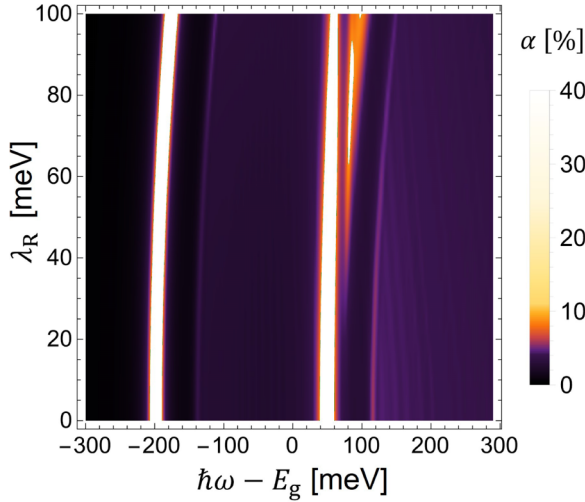


FIG. 4. Evolution of the absorption spectrum as Rashba SOC, λ_R , is increased from 0 to 100 meV. The parameters are the same as in Fig. 3.

showing that with increasing λ_R its height has increased and its position moves to higher energies. Importantly, there is no similar emergent Rashba-induced excitonic peaks close to the $A:1s$ excitonic transition. We address this point in the Appendix (Fig. 9). Moreover, unlike only a small increase in the height of the A peak, consistent with what is expected from the single-particle analysis in Fig. 2(b), we see that with increasing λ_R the spectral weight of the B peak is strongly reduced and transferred to the Rashba-induced peaks as shown in the inset. This difference between A - and B -exciton series is important for understanding better the microscopic mechanism that dominates the Rashba-induced modification of the optical response.

For a further view of the evolution of the A and B peaks along with multiple emergent peaks, in Fig. 4 we show a heat map that covers the evolution of the absorption spectrum as λ_R is increased from 0 to 100 meV. While in Fig. 3 we can already see that the B peak is accompanied by several satellite peaks, in Fig. 4 from a gradual decrease in the amplitude of the B peak it can be seen that it dissolves into several peaks. As λ_R increases, these emergent satellite peaks, at energies above the B peak, have a nonmonotonic spectral weight and position. This behavior leads to the overall broadening, as compared to the original B peak at $\lambda_R = 0$. At large λ_R there is a slightly decreased separation between A and B peaks, unlike the equal blueshifts expected from the single-particle analysis and denoted in Fig. 3.

3. Origin of emergent excitons: Mixing of excitonic states

While our previous analysis of the absorption spectra has focused on the k -space study of the excitonic features, complementary information is obtained from the real-space descriptions and the possibility to classify their symmetry, as suggested in Sec. II B. Combining k - and real-space descriptions of the excitons in CrX_3 has recently provided valuable information on the role of hybridization in the excitonic properties by changing X from Cl to Br and I [73]. Furthermore, the real-space exciton envelope function Eq. (9)

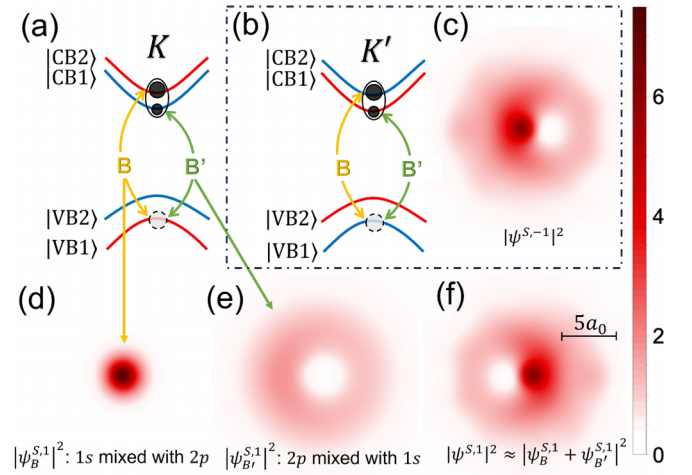


FIG. 5. (a), (b) Schematic illustration of the mixing of B and B' excitonic states, formed from both CBs and VB1, in the K and K' valley. (c), (f) Modulus squared of the real-space wave function as a function of $\mathbf{r}_e - \mathbf{r}_h$ for the Rashba-induced exciton in the K' and K valley with the energy $\Omega^{S,-1} = \Omega^{S,1} = 1.4789$ eV, from Eqs. (5) and (9). (d), (e) $|\psi_B^{S,1}|^2$ ($|\psi_{B'}^{S,-1}|^2$) as defined in Eq. (11): Modulus squared of $B(B')$ excitonic states formed from CB2 (CB1) and VB1 coupling, dominated by $1s$ ($2p$) state, in the K valley.

can be studied in detail by decomposing it into four parts according to the combination of subband indices c and v as

$$\Psi^{S,\tau}(\mathbf{r}_e - \mathbf{r}_h) = \Psi_A^{S,\tau}(\mathbf{r}_e - \mathbf{r}_h) + \Psi_{A'}^{S,\tau}(\mathbf{r}_e - \mathbf{r}_h) + \Psi_B^{S,\tau}(\mathbf{r}_e - \mathbf{r}_h) + \Psi_{B'}^{S,\tau}(\mathbf{r}_e - \mathbf{r}_h), \quad (11)$$

where A (A' , B , or B') corresponds to the summation over terms with $v, c = \text{VB2 (VB2, VB1, or VB1), CB1 (CB2, CB2, or CB1)}$ in Eq. (9). For example, $\Psi_A^{S,\tau}(\mathbf{r}_e - \mathbf{r}_h) = \sum_{\mathbf{k}} \mathcal{A}_{vck}^{S,\tau} \psi_{ck}^\tau(\mathbf{r}_e) \psi_{vk}^{\tau*}(\mathbf{r}_h)$ with $v = \text{VB2}, c = \text{CB1}$.

In the absence of Rashba SOC, each exciton is formed from only one CB and VB and can be labeled by the spin configuration of those bands. This is clear from the ground-state ($1s$) A or B excitons [recall Fig. 1(b)], which are formed from the electron-hole coupling exclusively from CB1 and VB2 or CB2 and VB1. They satisfy $\Psi^{S,\tau}(\mathbf{r}) = \Psi_A^{S,\tau}(\mathbf{r})$ and $\Psi^{S,\tau}(\mathbf{r}) = \Psi_B^{S,\tau}(\mathbf{r})$ separately with the exciton envelope wave function having either s -shell or p -shell symmetry; the latter is characterized by nonzero angular momentum. For nonzero λ_R , we focus on the emerging transition with the energy corresponding to the new peak in Fig. 3, which we call a Rashba-induced exciton. In Fig. 5 we present the modulus squared of the real-space envelope wave function of the Rashba-induced exciton. We see that for $\lambda_R = 50$ meV, $|\Psi^{S,\tau}|^2$ is neither a perfect s - nor a p -shell wave. It is asymmetrical along the x direction in both valleys. It is interesting to note that $|\Psi^{S,1}|^2$ and $|\Psi^{S,-1}|^2$ are related by reflection with respect to the y axis, a property that can be easily verified through step-by-step derivation starting from the effective Hamiltonian in Eq. (1).

The exciton envelope function $|\Psi^{S,\tau}|^2$ of a Rashba-induced exciton, which deviates from a conventional non-Rashba A/B exciton, can be understood by examining its four constituents, that is, $\Psi_A^{S,\tau}$, $\Psi_{A'}^{S,\tau}$, $\Psi_B^{S,\tau}$, and $\Psi_{B'}^{S,\tau}$. By comparing their contributions, we find that B and B' excitonic states dominate,

while a negligible amount of continuum A and A' states also contribute. Thus, a Rashba-induced exciton can be understood as the result of B and B' excitonic states mixing as summarized schematically in Figs. 5(a) and 5(b). Furthermore, B and B' excitonic states are $1s$ - and $2p$ -like, respectively, as shown by plots of their modulus squared wave functions in Figs. 5(d) and 5(e). We can clearly see in Fig. 5(e) that the B' excitonic state is not perfectly $2p$ -like but asymmetric due to $1s$ admixture. Similarly, the B excitonic state is predominately $1s$ with a small $2p$ contribution. The Rashba-induced excitonic state-mixing discussed above can be understood by careful examination of the BSE. Without Rashba, excitons consist only of excitations from one valence band to one conduction band because the kernel, Eq. (6), of the BSE, Eq. (5), is diagonal, i.e., proportional to $\delta_{c'c} \delta_{v,v'}$, where δ_{ij} denotes Kronecker symbols. As Rashba SOC is turned on, the kernel is no longer diagonal, and excitations between various valence and conduction bands couple to each other. This then leads to a mixing of previously decoupled states, which are close in energy, for example $B:1s$ (originally only from the transitions VB1 to CB2 for $\lambda_R = 0$) and $B':2p$ excitons (originally only from the transitions VB1 to CB1 for $\lambda_R = 0$). The mixing is the strongest for the states having close energies. For this reason, in particular, the Rashba-induced excitonic state is not visible for the A -series of excitons. The $A:1s$ and $A':2p$ states have larger energy mismatch. Likewise, the individual contributions B (CB2-VB1) and B' (CB1-BV1) also acquire small contributions from each other, while their main character is still mainly s - and p -like, respectively.

The obtained Rashba-induced exciton represents an additional microscopic mechanism contributing to the important class of excitonic s -shell and p -shell mixing phenomena. Let us emphasize several key physical ingredients, differentiating it from the previously studied scenario due to the symmetry reduction, considered in Ref. [74]. That prior work focused on the spin-allowed excitonic states (the dark excitons due to opposite spin states were neglected) and demonstrated that the $s - p$ mixing in the same valley can be achieved when accounting for the admixture of the remote bands. Using the $k \cdot p$ method beyond the axially symmetric model, it was shown that it is the admixture parameter (related to the interband matrix element of the momentum operator) with remote bands that gives rise to the mixing of $2s$ and $2p$ states and makes p -excitons optically active. In our case, the symmetry reduction is realized by means of the proximity-induced modification of the SOC, resulting in the appearance of the Rashba term. In our scheme, the $s - p$ mixing can be obtained without accounting for the remote bands and using only the minimal effective model of Dirac bands in TMDs. Interestingly, the Rashba-induced exciton is combined from $1s$ and $2p$ states with spin-allowed and spin-forbidden transitions, which contrasts the remote-band mechanism of the $s - p$ mixing from Ref. [74], requiring the same spin states.

Our analysis also confirms that the emergent excitons can be understood as the brightening of the dark states. However, compared to the previously studied case with a magnetic substrate where only the $1s$ excitons are brightened with an in-plane magnetization [26], there are several differences. With Rashba SOC-induced spin textures, a $B':2p$ (CB1-VB1) exciton remains optically forbidden, while it is the mixture

with a $B:1s$ (CB2-VB1) optically allowed state that brightens this exciton. Interestingly, even without Rashba SOC, mixing of $s - p$ states and an unusual excitonic structure was attributed to the presence of orbital textures in semiconductor nanostructures [75].

C. Trigonal warping

Similar to exploring the role of Rashba SOC on the absorption spectra, we also consider whether the presence of TW leads to observable changes. We again use BSE calculations where TW is described by Eq. (4). Even without considering a substrate, TW is inherent to the band structure in many 2D materials, including graphene [76], boron nitride [77], and TMD MLs [44]. The presence of TW leads to a threefold anisotropy in the band structure that directly influences different optical properties. For example, strong optical nonlinearities and second-harmonic generation are associated with TW as it breaks rotational symmetry [37]. Furthermore, TW can modify the chiral optical selection rules by changing the single-particle velocity matrix $D_{vck}^{\tau,\pm}$, and cause mixing of excitonic states [74,78].

To examine the influence of TW, we first show in Figs. 6(a) and 6(c) how it changes CB and VB isoenergy contours without and with Rashba SOC. While both in CB and VB there is a striking change from the isotropic band structure to a threefold anisotropy with TW, a further inclusion of Rashba SOC leads only to modest changes. Turning to the absorption spectra, our calculations in Figs. 6(b) and 6(d) show that for realistic TW strengths there are negligible changes on the excitonic spectra. In the absence of TW, spin-valley locking implies that at $k = 0$ each valley is associated with interband optical transitions with only a single helicity of light, while this locking is reduced at $k \neq 0$, allowing admixture with the other helicity [9]. With TW, spin-valley locking is further reduced.

For the considered calculations, where we include the contributions of the K and K' valleys, we conclude that neglecting the TW effects is an accurate approximation for the absorption spectra in ML TMDs. This conclusion is not a surprise considering that low-energy exciton wave functions in ML TMDs are highly localized around the K/K' points [60]. In contrast, TW is more pronounced far away from the K/K' points. This agrees with our conclusions that the influence of TW in the study of excitons is negligible, while it can be noticeable in the single-particle band structure.

D. Binding energy

One of the hallmarks of ML TMDs is the occurrence of tightly bound excitons, characterized by binding energies that can exceed 100 meV [1]. To investigate the effects of Rashba and TW on the stability of excitons, we explore the change of the ground state ($1s$) A exciton binding energy in Fig. 7. The binding energy of an exciton S in the τ valley is calculated as the difference in energy between a free and bound electron-hole pair,

$$E_b = \epsilon_c^\tau - \epsilon_v^\tau - \Omega^{S,\tau}, \quad (12)$$

where, as defined in Eq. (5), ϵ_c^τ (ϵ_v^τ) is the conduction- (valence-) band edge, and $\Omega^{S,\tau}$ is the exciton energy in the

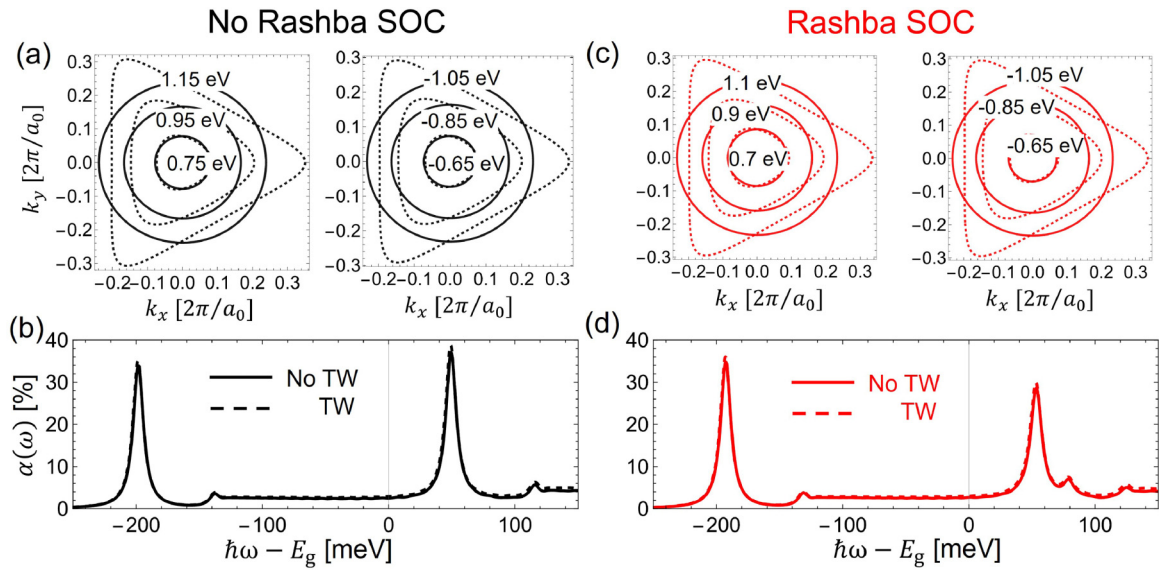


FIG. 6. Effect of trigonal warping (TW) on the band structures in the K valley and on the absorption spectra, in the absence of Rashba SOC (a) and (b). A similar analysis in the presence of Rashba SOC, $\lambda_R = 50$ meV in (c) and (d). Solid (dashed) lines represent the absence (presence) of TW. In (a), without Rashba SOC, the energy contours of CB1 and VB2 are shown separately and labeled by the corresponding positive and negative energies. Similarly, in (c), they are shown in the presence of Rashba SOC.

state S in the τ valley. For realistic values of Rashba SOC and TW, the binding energy, E_b , is increased by up to about 2 meV from the value of 70.3 meV, which was obtained without Rashba SOC and TW. This resulting small effect of Rashba SOC and TW on E_b suggests that the single-particle description of the changes in the band-edge position can accurately capture the shift of the excitonic peaks.

IV. CONCLUSIONS AND OUTLOOK

We have used a low-energy effective Hamiltonian and the resulting four-band model to study the influence of Rashba SOC and TW on the optical properties of ML TMDs. Both Rashba SOC and TW were found to strongly modify the

single-particle properties through creating noncollinear spin textures and forming a threefold anisotropy in the isoenergy contours, respectively. In contrast, by using the Bethe-Salpeter equation to calculate the optical absorption, we found a significant change for Rashba SOC, which leads to emergent excitons by coupling different conduction bands and mixing of $1s$ and $2p$ excitonic states. With TW the calculated changes on the absorption spectra are negligible.

The relative importance of Rashba SOC, as compared to TW, in the study of excitons comes from the localization of excitons around band edges K/K' [60]. The corresponding exciton wave functions are mainly affected by the dispersion around the K/K' points. The dispersion around the K/K' points, in turn, is strongly affected by Rashba SOC, which breaks the collinear spin alignment and introduces energy shifts at the band edges (recall Fig. 2). TW is, on the other hand, more pronounced far away from the K/K' points, and thus negligible in the study of excitons.

However, this situation, where the neglect of TW provides an accurate description of optical properties, is not universal. For example, TW can lead to strong nonlinearities [36–38] and important changes in the optical response when only a single valley is considered, or if there is an in-plane applied electric field. By changing such an electric field, which alters the overlap between conduction and valence bands [79], one can control the degree of circularly polarized light, which has been experimentally demonstrated in ML WSe₂, [80,81]. This mechanism could provide a modulation of spin polarization, suitable for proposed TMD-based spin-lasers [82].

Given the importance of excitons in the optical properties of ML TMDs, we expect that our analysis for the influence of Rashba SOC and TW will stimulate further studies as they are inherent to many systems. Specifically, the predicted presence of emergent excitons could be experimentally tested in Janus TMDs, as they support sufficiently strong Rashba SOC, for

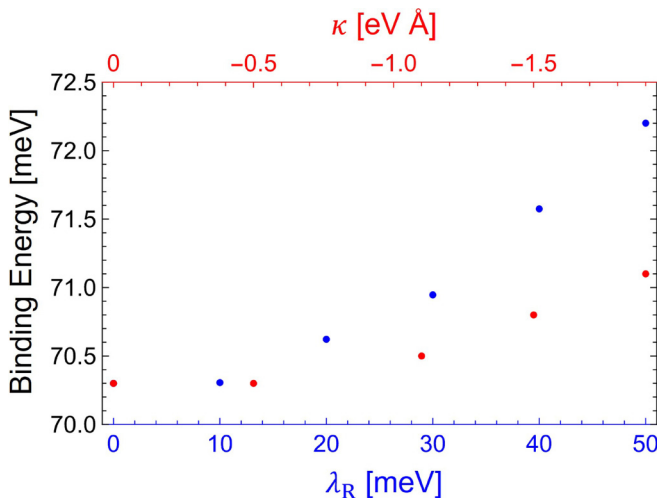


FIG. 7. Evolution of the binding energy for the ground state ($1s$) A exciton with TW and Rashba SOC, from Eq. (12).

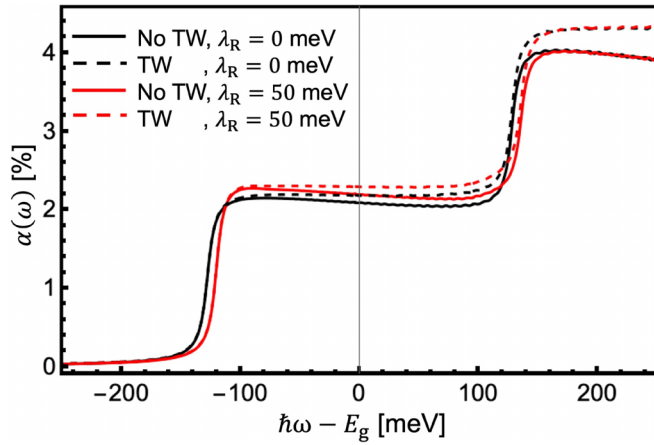


FIG. 8. Single-particle absorption spectra without and with Rashba SOC and TW. The remaining parameters correspond to those from Fig. 3.

example α_R in MoSSe (WSSe) is 77 meV (158 meV) [3]. It would be interesting to explore the role of strain [83] in the presence of Rashba SOC, as their interplay would change the optical response. Our work can also be viewed as a guidance to the analysis of various proximity effects, such as those due to magnetic or charge density wave substrates [16,26,84], which could directly modify the underlying excitonic features and be influenced by Rashba SOC and TW.

ACKNOWLEDGMENTS

This work is primarily supported by the U.S. Department of Energy, Office of Science, Basic Energy Sciences under Award No. DE-SC0004890 (I.Ž., J.D.C., and K.D.) and National Natural Science Foundation of China under Award No. 12104118 (G.X.). Computational resources were provided by the UB Center for Computational Research.

APPENDIX: SINGLE-PARTICLE ABSORPTION AND THE POSITION OF RASHBA-INDUCED PEAKS

By excluding Coulomb interaction, the resulting absorption spectra for air/MoTe₂/substrate in Fig. 8 show pronounced differences compared to previous many-body results obtained from BSE in Fig. 3. Instead of excitonic A and B peaks, there are two jumps in the absorption, corresponding

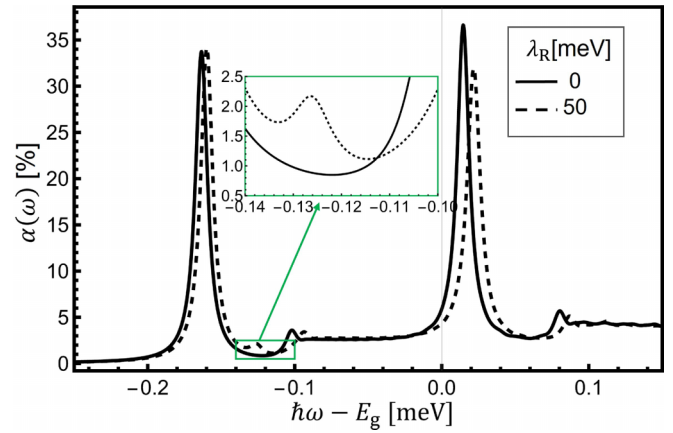


FIG. 9. Absorption spectrum without and with Rashba SOC ($\lambda_R = 0, 50$ meV). In each case the intrinsic CB SOC, $\lambda_c = 18$ meV, is reversed compared to the previous calculations. The inset highlights an emergent excitonic peak near the A exciton. The remaining parameters are the same parameters as in Fig. 3.

to the transitions between CB1 and VB2 and CB2 and VB1, respectively. These jumps are at different positions from the A and B peaks as they are not redshifted by the binding energies, E_b , as shown in Fig. 7, while the overall maximum in the absorption is nearly an order of magnitude smaller than in Fig. 3. The presence of Rashba SOC and TW leads to only small modifications in the single-particle absorption.

One striking feature of the emergent extra excitonic peaks is that they appear only after the B peak, but not the A peak, as can be seen in Figs. 3 and 4. A simple understanding of this property is that an energy match is necessary for the admixture of various states which form these emergent excitons. For example, the ground state of the B exciton has a larger energy than that of the B' exciton. Hence it is possible to have an admixture between $1s$ of the B exciton and $2p$ of the B' exciton. In contrast, due to the band ordering, determined by the intrinsic SOC parameters λ_c and λ_v , there is no such admixture between $1s$ of the A exciton and $2p$ of the A' exciton. Our understanding is verified in Fig. 9, where our previous calculations are repeated by artificially reversing the band ordering of the CBs by imposing $\lambda_c \rightarrow -\lambda_c$ which leads to an extra peak after the A peak rather than the B peak.

- [1] G. Wang, A. Chernikov, M. M. Glazov, T. F. Heinz, X. Marie, T. Amand, and B. Urbaszek, Colloquium: Excitons in atomically thin transition metal dichalcogenides, *Rev. Mod. Phys.* **90**, 021001 (2018).
- [2] A. Carvalho, M. Weng, X. Zhu, A. S. Rodin, H. Su, and A. H. C. Neto, Phosphorene: from theory to applications, *Nat. Rev. Mater.* **1**, 16061 (2016).
- [3] X. Tang and L. Kou, 2D Janus transition metal dichalcogenides: Properties and applications, *Phys. Status Solidi B* **259**, 210000562 (2022).
- [4] M. Syperek, R. Stühler, A. Consiglio, P. Holewa, P. Wyborski, L. Dusanowski, F. Reis, S. Höfling, R. Thomale, W. Hanke, R.

Claessen, D. Di Sante, and C. Schneider, Observation of room temperature excitons in an atomically thin topological insulator, *Nat. Commun.* **13**, 6313 (2022).

- [5] T. Woźniak, Umm-e-hani, P. E. Faria, Jr., M. S. Ramzan, and A. B. Kuc, Electronic and excitonic properties of MSi₂Z₄ monolayers, *Small* **19**, 2206444 (2023).
- [6] A. N. Rudenko, S. Acharya, F. Tasnádi, D. Pashov, A. V. Ponomareva, M. van Schilfgaarde, I. A. Abrikosov, and M. I. Katsnelson, Electronic and optical properties of crystalline nitrogen versus black phosphorus: A comparative first-principles study, *Phys. Rev. B* **105**, 205135 (2022).

- [7] M. Grzeszczyk, S. Acharya, D. Pashov, Z. Chen, K. Vaklinova, M. van Schilfgaarde, K. Watanabe, T. Taniguchi, K. S. Novoselov, M. I. Katsnelson, and M. Koperski, Strongly correlated exciton-magnetization system for optical spin pumping in CrBr₃ and CrI₃, *Adv. Mater.* **35**, 2209513 (2023).
- [8] D. Y. Qiu, F. H. da Jornada, and S. G. Louie, Optical spectrum of MoS₂: Many-body effects and diversity of exciton states, *Phys. Rev. Lett.* **111**, 216805 (2013).
- [9] D. Xiao, G.-B. Liu, W. Feng, X. Xu, and W. Yao, Coupled spin and valley physics in monolayers of MoS₂ and other group-VI dichalcogenides, *Phys. Rev. Lett.* **108**, 196802 (2012).
- [10] A. Chernikov, T. C. Berkelbach, H. M. Hill, A. Rigosi, Y. Li, B. Aslan, D. R. Reichman, M. S. Hybertsen, and T. F. Heinz, Exciton binding energy and nonhydrogenic Rydberg series in monolayer WS₂, *Phys. Rev. Lett.* **113**, 076802 (2014).
- [11] M. Amani, D.-H. Lien, D. Kiriya, J. Xiao, A. Azcatl, J. Noh, S. R. Madhupathy, R. Addou, S. KC, M. Dubey, K. Cho, R. M. Wallace, S.-C. Lee, J.-H. He, J. W. Ager, X. Zhang, E. Yablonovitch, and A. Javey, Near-unity photoluminescence quantum yield in MoS₂, *Science* **350**, 1065 (2015).
- [12] K. F. Mak and J. Shan, Photonics and optoelectronics of 2D semiconductor transition metal dichalcogenides, *Nat. Photon.* **10**, 216 (2016).
- [13] C. Zhao, T. Norden, P. Zhao, Y. Cheng, P. Zhang, F. Sun, P. Taheri, J. Wang, Y. Yang, T. Scrace, K. Kang, S. Yang, G. Miao, R. Sabirianov, G. Kioseoglou, A. Petrou, and H. Zeng, Enhanced valley splitting in monolayer WSe₂ due to magnetic exchange field, *Nat. Nanotechnol.* **12**, 757 (2017).
- [14] D. Zhong, K. L. Seyler, X. Linpeng, R. Cheng, N. Sivadas, B. Huang, E. Schmidgall, T. Taniguchi, K. Watanabe, M. A. McGuire, W. Yao, D. Xiao, K.-M. C. Fu, and X. Xu, Van der Waals engineering of ferromagnetic semiconductor heterostructures for spin and valleytronics, *Sci. Adv.* **3**, e1603113 (2017).
- [15] I. Žutić, A. Matos-Abiague, B. Scharf, H. Dery, and K. Belashchenko, Proximitized materials, *Mater. Today* **22**, 85 (2019).
- [16] J. Joshi, B. Scharf, I. Mazin, S. Krylyuk, D. J. Campbell, J. Paglione, A. Davydov, I. Žutić, and P. M. Vora, Charge density wave activated excitons in TiSe₂-MoSe₂ heterostructures, *APL Mater.* **10**, 011103 (2022).
- [17] M. Bora and P. Deb, Magnetic proximity effect in two-dimensional van der Waals heterostructure, *J. Phys. Mater.* **4**, 034014 (2021).
- [18] D. Zhong, K. L. Seyler, X. Linpeng, N. P. Wilson, T. Taniguchi, K. Watanabe, M. A. McGuire, K.-M. C. Fu, D. Xiao, W. Yao, and X. Xu, Layer-resolved magnetic proximity effect in van der Waals heterostructures, *Nat. Nanotechnol.* **15**, 187 (2020).
- [19] Q.-Q. Zhang, Q. Li, X.-T. An, and J.-J. Liu, Valley-resolved quantum anomalous Hall effect in ferromagnetically proximitized monolayer MoTe₂, *Phys. Rev. B* **105**, 205436 (2022).
- [20] Y. Saito, Y. Nakamura, M. S. Bahrany, Y. Kohama, J. Ye, Y. Kasahara, Y. Nakagawa, M. Onga, M. Tokunaga, T. Nojima, Y. Yanase, and Y. Iwasa, Superconductivity protected by spin-valley locking in ion-gated MoS₂, *Nat. Phys.* **12**, 144 (2016).
- [21] N. Cortés, O. Ávalos-Ovando, L. Rosales, P. A. Orellana, and S. E. Ulloa, Tunable spin-polarized edge currents in proximitized transition metal dichalcogenides, *Phys. Rev. Lett.* **122**, 086401 (2019).
- [22] V. Zatko, M. Galbiati, S. Mutien-Marie Dubois, M. Och, P. Palczynski, C. Mattevi, P. Brus, O. Bezenenet, M.-B. Martin, B. Servet, J.-C. Charlier, F. Godel, A. Vecchiola, K. Bouzouhane, S. Collin, F. Petroff, B. Dlubak, and P. Seneor, Band-structure spin-filtering in vertical spin valves based on chemical vapor deposited WS₂, *ACS Nano* **13**, 14468 (2019).
- [23] Z. Tu, T. Zhou, T. Ersevım, H. S. Arachchige, A. T. Hanbicki, A. L. Friedman, D. Mandrus, M. Ouyang, I. Žutić, and C. Gong, Spin-orbit coupling proximity effect in MoS₂/Fe₃GeTe₂ heterostructures, *Appl. Phys. Lett.* **120**, 043102 (2022).
- [24] K. Dolui and B. K. Nikolić, Spin-orbit-proximitized ferromagnetic metal by monolayer transition metal dichalcogenide: Atlas of spectral functions, spin textures, and spin-orbit torques in Co/MoSe₂, Co/WSe₂, and Co/TaSe₂ heterostructures, *Phys. Rev. Mater.* **4**, 104007 (2020).
- [25] X. Zhang, W.-Y. Shan, and D. Xiao, Optical selection rule of excitons in gapped chiral fermion systems, *Phys. Rev. Lett.* **120**, 077401 (2018).
- [26] B. Scharf, G. Xu, A. Matos-Abiague, and I. Žutić, Magnetic proximity effects in transition-metal dichalcogenides: Converting excitons, *Phys. Rev. Lett.* **119**, 127403 (2017).
- [27] G. Xu, T. Zhou, B. Scharf, and I. Žutić, Optically probing tunable band topology in atomic monolayers, *Phys. Rev. Lett.* **125**, 157402 (2020).
- [28] A. Gloppe, M. Onga, R. Hisatomi, A. Imamoglu, Y. Nakamura, Y. Iwasa, and K. Usami, Magnon-exciton proximity coupling at a van der Waals heterointerface, *Phys. Rev. B* **105**, L121403 (2022).
- [29] J. C. G. Henriques, G. Catarina, A. T. Costa, J. Fernández-Rossier, and N. M. R. Peres, Excitonic magneto-optical Kerr effect in 2D transition metal dichalcogenides induced by spin proximity, *Phys. Rev. B* **101**, 045408 (2020).
- [30] M. Onga, Y. Sugita, T. Ideue, Y. Nakagawa, R. Suzuki, Y. Motome, and Y. Iwasa, Antiferromagnet-semiconductor van der Waals heterostructures: Interlayer interplay of exciton with magnetic ordering, *Nano Lett.* **20**, 4625 (2020).
- [31] A. C. Dias, H. Braganca, H. Zeng, A. L. A. Fonseca, D.-S. Liu, and F. Qu, Large room-temperature valley polarization by valley-selective switching of exciton ground state, *Phys. Rev. B* **101**, 085406 (2020).
- [32] D. Wang and X. Zou, Tunable valley band and exciton splitting by interlayer orbital hybridization, *npj Comput. Mater.* **8**, 239 (2022).
- [33] D. Bercioux and P. Lucignano, Quantum transport in Rashba spin-orbit materials: A review, *Rep. Prog. Phys.* **78**, 106001 (2015).
- [34] I. Žutić, J. Fabian, and S. Das Sarma, Spintronics: Fundamentals and applications, *Rev. Mod. Phys.* **76**, 323 (2004).
- [35] J. Chen, K. Wu, H. Ma, W. Hu, and J. Yang, Tunable Rashba spin splitting in Janus transition-metal dichalcogenide monolayers via charge doping, *RSC Adv.* **10**, 6388 (2020).
- [36] F. Mahmoudi and R. Asgari, Nonreciprocal photocurrent in the nonlinear response of two-dimensional models, *Phys. Rev. B* **105**, 085403 (2022).
- [37] A. Säynätjoki, L. Karvonen, H. Rostami, A. Autere, S. Mehravar, A. Lombardo, R. A. Norwood, T. Hasan, N. Peyghambarian, H. Lipsanen, K. Kieu, A. C. Ferrari, M. Polini, and Z. Sun, Ultra-strong nonlinear optical processes and trigonal warping in MoS₂ layers, *Nat. Commun.* **8**, 893 (2017).
- [38] Y. V. Zhumagulov, V. D. Neverov, A. E. Lukyanov, D. R. Gulevich, A. V. Krasavin, A. Vagov, and V. Perebeinos,

- Nonlinear spectroscopy of excitonic states in transition metal dichalcogenides, *Phys. Rev. B* **105**, 115436 (2022).
- [39] C. F. Klingshryn, *Semiconductor Optics*, 4th ed. (Springer, New York, 2012).
- [40] T. Ando, T. Nakanishi, and R. Saito, Berry's phase and absence of back scattering in carbon nanotubes, *J. Phys. Soc. Jpn.* **67**, 2857 (1998).
- [41] M. S. Dresselhaus and G. Dresselhaus, Intercalation compounds of graphite, *Adv. Phys.* **51**, 1 (2002).
- [42] H. Rostami, A. G. Moghaddam, and R. Asgari, Effective lattice Hamiltonian for monolayer MoS₂: Tailoring electronic structure with perpendicular electric and magnetic fields, *Phys. Rev. B* **88**, 085440 (2013).
- [43] A. Kormányos, V. Zólyomi, N. D. Drummond, P. Rakytá, G. Burkard, and V. I. Fal'ko, Monolayer MoS₂: Trigonal warping, the Γ valley, and spin-orbit coupling effects, *Phys. Rev. B* **88**, 045416 (2013).
- [44] A. Kormányos, G. Burkard, M. Gmitra, J. Fabian, V. Zólyomi, N. D. Drummond, and V. Fal'ko, $k \cdot p$ theory for two-dimensional transition metal dichalcogenide semiconductors, *2D Mater.* **2**, 022001 (2015).
- [45] Y. A. Korkmaz, C. Bulutay, and C. Sevik, $k \cdot p$ parametrization and linear and circular dichroism in strained monolayer (Janus) transition metal dichalcogenides from first-principles, *J. Phys. Chem. C* **125**, 7439 (2021).
- [46] J. Choi, C. Lane, J.-X. Zhu, and S. A. Crooker, Asymmetric magnetic proximity interactions in MoSe₂/CrBr₃ van der Waals heterostructures, *Nat. Mater.* **22**, 305 (2023).
- [47] T. Zhou and I. Žutić, Asymmetry in the magnetic neighbourhood, *Nat. Mater.* **22**, 284 (2023).
- [48] J. Fabian, A. Matos-Abiague, C. Ertler, P. Stano, and I. Žutić, Semiconductor spintronics, *Acta Phys. Slov.* **57**, 565 (2007).
- [49] W. Hanke and L. J. Sham, Local-field and excitonic effects in the optical spectrum of a covalent crystal, *Phys. Rev. B* **12**, 4501 (1975).
- [50] W. Hanke and L. J. Sham, Many-particle effects in the optical spectrum of a semiconductor, *Phys. Rev. B* **21**, 4656 (1980).
- [51] M. Rohlfing and S. G. Louie, Electron-hole excitations and optical spectra from first principles, *Phys. Rev. B* **62**, 4927 (2000).
- [52] B. Scharf, T. Frank, M. Gmitra, J. Fabian, I. Žutić, and V. Perebeinos, Excitonic stark effect in MoS₂ monolayers, *Phys. Rev. B* **94**, 245434 (2016).
- [53] L. V. Keldysh, Coulomb interaction in thin semiconductor and semimetal films, *Pis'ma Zh. Eksp. Teor. Fiz.* **29**, 716 (1979) [*JETP Lett.* **29**, 658 (1979)].
- [54] P. Cudazzo, I. V. Tokatly, and A. Rubio, Dielectric screening in two-dimensional insulators: Implications for excitonic and impurity states in graphene, *Phys. Rev. B* **84**, 085406 (2011).
- [55] M. F. C. M. Quintela, J. C. G. Henriques, L. G. M. Tenório, and N. M. R. Peres, Theoretical methods for excitonic physics in 2D materials, *Phys. Status Solidi B* **259**, 2200097 (2022).
- [56] C. Zhang, H. Wang, W. Chan, C. Manolatou, and F. Rana, Absorption of light by excitons and trions in monolayers of metal dichalcogenide MoS₂: Experiments and theory, *Phys. Rev. B* **89**, 205436 (2014).
- [57] D. Van Tuan, B. Scharf, Z. Wang, J. Shan, K. F. Mak, I. Žutić, and H. Dery, Probing many-body interactions in monolayer transition-metal dichalcogenides, *Phys. Rev. B* **99**, 085301 (2019).
- [58] T. C. Berkelbach, M. S. Hybertsen, and D. R. Reichman, Theory of neutral and charged excitons in monolayer transition metal dichalcogenides, *Phys. Rev. B* **88**, 045318 (2013).
- [59] T. C. Berkelbach, M. S. Hybertsen, and D. R. Reichman, Bright and dark singlet excitons via linear and two-photon spectroscopy in monolayer transition-metal dichalcogenides, *Phys. Rev. B* **92**, 085413 (2015).
- [60] D. Y. Qiu, F. H. da Jornada, and S. G. Louie, Screening and many-body effects in two-dimensional crystals: Monolayer MoS₂, *Phys. Rev. B* **93**, 235435 (2016).
- [61] Z. Ye, T. Cao, K. O'Brien, H. Zhu, X. Yin, Y. Wang, S. G. Louie, and X. Zhang, Probing excitonic dark states in single-layer tungsten disulphide, *Nature (London)* **513**, 214 (2014).
- [62] Which is smooth and different from Figs. 3(b) and 3(c) in Ref. [8].
- [63] A. Arora, R. Schmidt, R. Schneider, M. R. Molas, I. Breslavetz, M. Potemski, and R. Bratschitsch, Valley Zeeman splitting and valley polarization of neutral and charged excitons in monolayer MoTe₂ at high magnetic fields, *Nano Lett.* **16**, 3624 (2016).
- [64] J. Qi, X. Li, Q. Niu, and J. Feng, Giant and tunable valley degeneracy splitting in MoTe₂, *Phys. Rev. B* **92**, 121403(R) (2015).
- [65] In Ref. [64], λ_R is obtained through comparing the band gap and splitting from the low-energy effective Hamiltonian with first-principles calculations.
- [66] G. D. Wilk, R. M. Wallace, and J. M. Anthony, High- κ gate dielectrics: Current status and materials properties considerations, *J. Appl. Phys.* **89**, 5243 (2001).
- [67] S. McDonnell, B. Brennan, A. Azcatl, N. Lu, H. Dong, C. Buie, J. Kim, C. L. Hinkle, M. J. Kim, and R. M. Wallace, HfO₂ on MoS₂ by atomic layer deposition: Adsorption mechanisms and thickness scalability, *ACS Nano* **7**, 10354 (2013).
- [68] S. Zhang, R. Liang, J. Wang, W. Chen, W. Cheng, L. Zhao, C. Sun, and J. Xu, Dependence of channel thickness on MoTe₂ transistor performance with Pt contact on a HfO₂ dielectric, *Appl. Phys. Express* **12**, 124001 (2019).
- [69] E. L. Ivchenko, *Optical Spectroscopy of Semiconductor Nanostructures* (Alpha Science, Harrow, UK, 2005).
- [70] E. I. Rashba, Properties of semiconductors with an extremum loop. 1. Cyclotron and combinational resonance in a magnetic field perpendicular to the plane of the loop, *Fiz. Tverd. Tela* **2**, 1224 (1960) [*Sov. Phys. Solid State* **2**, 1109 (1960)].
- [71] M. Inglot, V. K. Dugaev, E. Y. Sherman, and J. Barnaś, Optical spin injection in graphene with Rashba spin-orbit interaction, *Phys. Rev. B* **89**, 155411 (2014).
- [72] P. Y. Yu and M. Cardona, *Fundamentals of Semiconductors: Physics and Materials Properties*, 4th ed. (Springer, Berlin, 2010).
- [73] S. Acharya, D. Pashov, A. Rudenko, M. Rösner, M. van Schilfgarde, and M. Katsnelson, Real- and momentum-space description of the excitons in bulk and monolayer chromium tri-halides, *npj 2D Mater. Appl.* **6**, 33 (2022).
- [74] M. M. Glazov, L. E. Golub, G. Wang, X. Marie, T. Amand, and B. Urbaszek, Intrinsic exciton-state mixing and nonlinear optical properties in transition metal dichalcogenide monolayers, *Phys. Rev. B* **95**, 035311 (2017).

- [75] J. Lee, K. Vyborny, J. E. Han, and I. Žutić, Nodal ‘ground state’ and orbital textures in quantum dots, *Phys. Rev. B* **89**, 045315 (2014).
- [76] A. H. Castro Neto, F. Guinea, N. M. R. Peres, K. S. Novoselov, and A. K. Geim, The electronic properties of graphene, *Rev. Mod. Phys.* **81**, 109 (2009).
- [77] T. Galvani, F. Paleari, H. P. C. Miranda, A. Molina-Sánchez, L. Wirtz, S. Latil, H. Amara, and F. Ducastelle, Excitons in boron nitride single layer, *Phys. Rev. B* **94**, 125303 (2016).
- [78] P. Gong, H. Yu, Y. Wang, and W. Yao, Optical selection rules for excitonic Rydberg series in the massive Dirac cones of hexagonal two-dimensional materials, *Phys. Rev. B* **95**, 125420 (2017).
- [79] S. Wang, M. S. Ukhary, and R. Saito, Strain effect on circularly polarized electroluminescence in transition metal dichalcogenides, *Phys. Rev. Res.* **2**, 033340 (2020).
- [80] Y. J. Zhang, T. Oka, J. T. Ye, and Y. Iwasa, Electrically switchable chiral light-emitting transistor, *Science* **344**, 725 (2014).
- [81] J. F. G. Marin, D. Unuchek, Z. Sun, C. Y. Cheon, F. Tagarelli, K. Watanabe, T. Taniguchi, and A. Kis, Room-temperature electrical control of polarization and emission angle in a cavity-integrated 2D pulsed LED, *Nat. Commun.* **13**, 4884 (2022).
- [82] J. Lee, S. Bearden, E. Wasner, and I. Žutić, Spin-lasers: From threshold reduction to large-signal analysis, *Appl. Phys. Lett.* **105**, 042411 (2014).
- [83] K. Zollner, Paulo E. Faria Junior, and J. Fabian, Strain-tunable orbital, spin-orbit, and optical properties of monolayer transition-metal dichalcogenides, *Phys. Rev. B* **100**, 195126 (2019).
- [84] L. Chirolli, Brightening odd-parity excitons in transition-metal dichalcogenides: Rashba spin-orbit interaction, skyrmions, and cavity polaritons, *Phys. Rev. B* **101**, 075426 (2020).

Correction: Support information in the Acknowledgment section was incomplete and has been fixed.